J. of Cardiovasc. Trans. Res. (2011) 4:477–492
DOI 10.1007/s12265-011-9275-1

Emerging MRI Methods in Translational Cardiovascular Research

Moriel H. Vandsburger · Frederick H. Epstein

Received: 23 February 2011 / Accepted: 15 March 2011 / Published online: 31 March 2011

Abstract Cardiac magnetic resonance imaging (CMR) has become a reference standard modality for imaging of left ventricular (LV) structure and function and, using late gadolinium enhancement, for imaging myocardial infarction. Emerging CMR techniques enable a more comprehensive examination of the heart, making CMR an excellent tool for use in translational cardiovascular research. Specifically, emerging CMR methods have been developed to measure the extent of myocardial edema, changes in ventricular mechanics, changes in tissue composition as a result of fibrosis, and changes in myocardial perfusion as a function of both disease and infarct healing. New CMR techniques also enable the tracking of labeled cells, molecular imaging of biomarkers of disease, and changes in calcium flux in cardiomyocytes. In addition, MRI can quantify blood flow velocity and wall shear stress in large blood vessels. Almost all of these techniques can be applied in both pre-clinical and clinical settings, enabling both the techniques themselves and the knowledge gained using such techniques in pre-clinical research to be translated from the lab bench to the patient bedside.

Keywords MRI · Myocardial infarction · Perfusion · Fibrosis · Molecular imaging · Calcium

M. H. Vandsburger
Department of Biological Regulation,
Weizmann Institute of Science,
76100 Rehovot, Israel
e-mail: moriel.vandsburger@gmail.com

F. H. Epstein (✉)
Departments of Radiology, Biomedical Engineering, and
Cardiovascular Research Center, University of Virginia,
PO Box 800759, 480 Ray C. Hunt Drive,
Charlottesville, VA 22908, USA
e-mail: fredepstein@virginia.edu

Introduction

Diseases of the heart, including myocardial infarction (MI) and heart failure, continue to be a leading cause of morbidity and mortality in the western world. In the USA alone, over five million people receive medical care for heart failure each year at a cost of tens of billions of dollars [1]. Research into the mechanisms of and potential therapies for cardiovascular disease has increasingly relied upon the use of animal models, with the ultimate goal of translating discoveries from the lab bench to the clinic. Similarities between mice and humans in terms of cardiovascular structure and function, physiology, and healing and remodeling of the left ventricle (LV) after MI coupled with both the ability to manipulate the mouse genome and the relatively low cost of mouse research underlie the extensive use of mouse models in cardiovascular translational research. Current efforts to develop novel therapies for patient treatment, including cell- [2, 3], gene- [4], biomaterial- [5], and microRNA- [6] based therapies, will be evaluated extensively in small animal models prior to translation to human use.

Traditionally, preclinical cardiovascular research has relied upon in vitro techniques such as immunohistochemistry of isolated tissue sections and examination of individual cells for assessment of diseases and treatments. In addition, invasive in vivo techniques, such as the use of LV pressure catheters, have been used to study LV function. While these techniques are very useful for multi-scale characterization of the heart, they have limitations such as being poorly suited for sequential measurements. To complement conventional methods, a variety of non-invasive and minimally invasive in vivo imaging methods have been investigated for small animals. For example, echocardiography using high-frequency transducers has

been used to measure LV structure and function. Also, PET imaging is useful for assessment of metabolism and targeted molecular imaging [7]; and in vivo bioluminescence imaging has become a standard by which to image changes in gene expression using conditional expression of reporter genes.

For the evaluation of cardiac structure and function, MRI has become a reference standard modality for essentially all species ranging from mice to humans [8–10]. Cardiac MRI (CMR) offers a combination of high spatial resolution and high soft tissue contrast. As a result, CMR has been used extensively to image the heart in terms of LV structure and function, and also to identify the extent of MI [11, 12], and to measure myocardial perfusion [9]. In addition, newer CMR methods can assess fibrosis, myocardial edema, certain cells, and calcium channel function in preclinical and/or clinical research. This review will focus on current and emerging CMR methods for translational cardiovascular research. Specifically, this review will discuss CMR of LV structure and contractile function, contrast-enhanced CMR of MI and fibrosis, CMR of myocardial edema, CMR of myocardial perfusion, MRI of cell tracking and targeted molecular imaging, manganese-enhanced (Mn-enhanced) MRI of calcium (Ca^{2+}) channel function, and finally MRI of blood flow and wall shear stress in large blood vessels.

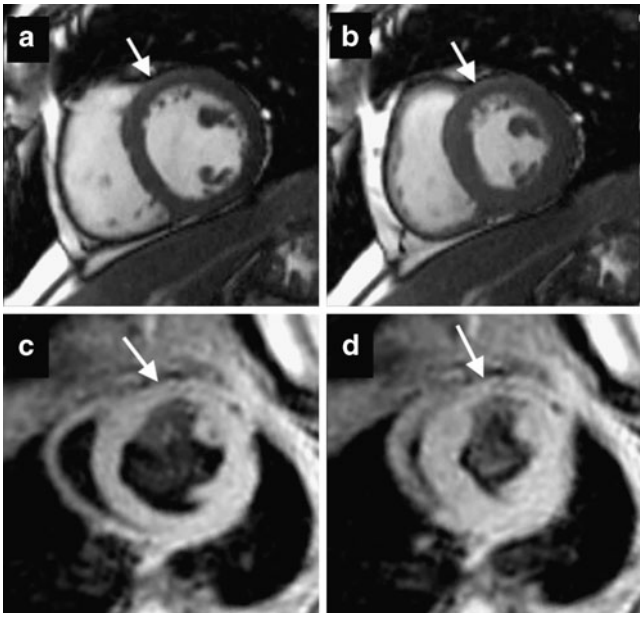

Fig. 1 Cine CMR of LV structure and function in a human patient and a mouse. Post-infarct cine images acquired at end diastole (ED) (**a**) and end systole (ES) (**b**) in a human, and at ED (**c**) and ES (**d**) in a mouse. Blood appears dark in **c** and **d** due to the use of a dark-blood magnetization preparation [137]. Thinning of the anterior wall of the LV can be seen (*white arrows*) in both the patient and the mouse at ED and ES. At ES, the thinned infarct zone demonstrates akinesis compared to noninfarcted myocardium in both the patient and the mouse. Human images were reprinted with permission from Salerno and Kramer [9]

MRI of Left Ventricular Structure and Function

Changes in the structure and function of the heart, which typically manifest as increases in LV volume, thinning or thickening of the LV wall, regional wall motion abnormalities, and decreases in LV ejection fraction (EF) are typical of the diseased heart [9]. Due to its superb image quality in terms of spatial and temporal resolution, image contrast, and lack of artifacts, cine CMR is well-established for the measurement of LV volumes, wall thickness, and EF [8, 9, 13, 14]. Example end-diastolic and end-systolic CMR images acquired after MI in a patient and a mouse are shown in Fig. 1, and illustrate the ability to visualize changes in wall thickness and LV function in both clinical and preclinical settings. Clinically, cine CMR is routinely used to identify ischemic [9] and non-ischemic cardiomyopathy [15].

Over the past 20 years, several MRI techniques which enable measurement of regional myocardial displacement and strain have been developed, including myocardial tagging [16, 17], and more recently *d*isplacement *en*coding with *s*timulated *e*choes (DENSE) [18–24]. In the mammalian heart, mid-wall cardiac myofibers are circumferentially oriented [25, 26]. As such, measurements of mid-wall circumferential shortening (E_{cc}) and rate of circumferential shortening provide in vivo measurements that reflect cardiomyocyte shortening and shortening velocity, respectively [27]. Myocardial tagging is a well-established technique [16, 17, 28] and has been used extensively in studies ranging from small animals [21, 27, 29, 30] to patients [28, 31]. For example, we recently used myocardial tagging in mice to quantify regional contractile function after MI [17, 21, 32], as well as to elucidate the roles of individual genes in modulating contractile function in transgenic [32] and knockout mice [21, 27]. Myocardial tagging has also been used to assess mesenchymal stem cell therapy in porcine models of acute and chronic MI [33, 34], as well as changes in regional E_{cc} after MI in humans [28, 35]. A recent myocardial tagging study demonstrated similar patterns of circumferential and radial strain in rodents and humans with the magnitude of strain increasing with the size of the heart, as well as a consistent transmural E_{cc} gradient across species [36]. Such findings both illustrate the translational capacity of myocardial tagging and demonstrate the utility that measurement of myocardial strain can play in determining the translational potential of novel therapies.

Cine DENSE MRI, which is an emerging technique that builds on some of the concepts that underlie myocardial tagging, has been used to measure myocardial displacement and strain with higher spatial resolution in mice [19, 20],

and humans [18, 22–24, 37]. In this technique, tissue displacement is encoded into the phase of the stimulated echo and phase images essentially directly record tissue motion at high spatial resolution. Using multiple orthogonal measurements, both 2- and 3D myocardial mechanics can be measured, as demonstrated recently in humans [24, 38]. Sample images from cine-DENSE acquisitions in a human and a mouse, both after MI, are shown in Fig. 2. In both humans and mice, reduced displacement and circumferential strain in infarct zone myocardium were measured using cine DENSE. An immediate clinical application of 3D cine DENSE may be the measurement of LV torsion in patients with diastolic dysfunction [39], a condition in which systolic function is preserved but diastole and untwisting of the LV is impaired [40]. Compared to other aspects of heart failure, diastolic dysfunction is less well understood [40]. A better understanding of the causes and characteristics of diastolic dysfunction may help to both improve diagnosis of affected patients and to direct development of potential treatments.

MRI of Myocardial Infarction, Fibrosis, and Edema

The ability to visualize the presence and extent of MI, evaluate myocardial viability, and quantify myocardial infarct size using CMR with gadolinium-based contrast agents has been a major advance in cardiac imaging [11, 12]. After intravenous injection, gadolinium (which enhances the relaxation rate of neighboring water molecules) quickly washes out of healthy myocardium while remaining trapped within areas of acute MI and scar tissue. Subsequently, T1-weighted MR imaging at an appropriately chosen inversion time (TI) [41] yields images with infarct zone hyperintensity. This technique, which is often referred to as delayed contrast-enhanced or late gadolinium enhanced (LGE)-CMR, is used regularly in both patients [9, 11] and in animal models of MI [21, 29, 42] to confirm the presence and measure the extent of both acute and chronic MI (Fig. 3).

While LGE CMR of dense fibrosis is now well-established (Fig. 4), identification of diffuse fibrosis with gadolinium-enhanced CMR is an emerging method. Diffuse interstitial fibrosis promotes a progression towards heart failure [43] and increases the likelihood of ventricular arrhythmias [44]. The current gold standard for diagnosis of myocardial fibrosis, measurement of collagen volume fraction (CVF) in heart biopsy samples [45], is invasive and forces clinicians to make assumptions about non-biopsied areas based on a small sample of myocardium. Recently, measurement of gadolinium-enhanced myocardial T1 relaxation times distinguished healthy myocardium from areas of diffuse fibrosis [43]. Gadolinium-enhanced MRI of diffuse fibrosis must be performed carefully, as this method can be effected by choice of pulse sequence, method of gadolinium administration, and glomerular filtration rate [46]. While these methods continue to evolve, quantification of the gadolinium distribution volume (GDV), an in

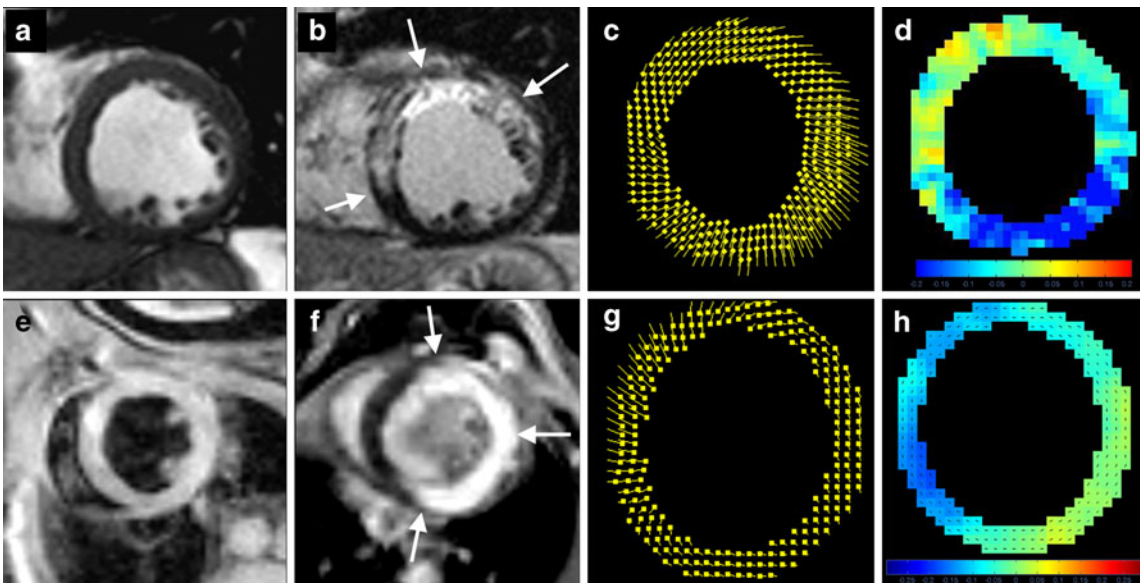

Fig. 2 Cine DENSE MRI of human and mouse hearts after myocardial infarction (MI). **a** End diastolic, mid-ventricular short axis image of the human heart. **b** Late gadolinium enhanced (LGE) CMR image, in which infarcted myocardium appears hyperintense (*white arrows*) as compared to dark non-infarcted myocardium, indicating the location and extent of MI. **c** The corresponding end-systolic displacement map demonstrates regionally reduced displacement in close spatial-agreement to the region of infarction as defined in (**b**). **d** Similarly, the map of end-systolic circumferential shortening (E_{cc}) demonstrates regionally reduced E_{cc} in the infarcted zone. Similar results are seen in the mouse heart (**e**–**h**) following surgically induced reperfused MI

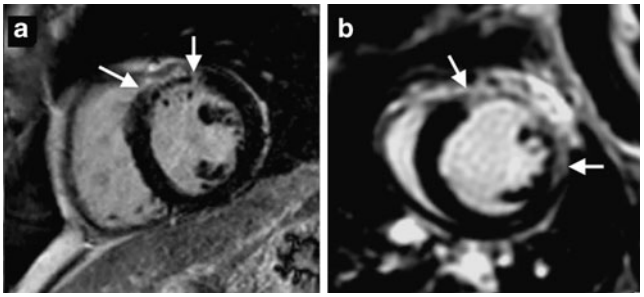

Fig. 3 LGE CMR images of MI in a human (**a**) and a mouse (**b**). Images were acquired using inversion recovery pulse sequences. Regions which appear hyperintense (*white arrows*) represent areas of infarcted myocardium. **a** A dark area is seen at the core of the infarct, representing a region of microvascular obstruction. **b** Enhancement of the infarcted anterior wall is transmural. Figure components reprinted with permission from Salerno and Kramer [9]

vivo surrogate of CVF, appear most promising [45, 47, 48]. In an initial in vitro study, the T1 of myocardial samples stored in saline was measured before and 24 h after incubation with gadolinium [45]. GDV, which was measured as the change in T1 relaxation of tissue normalized to the change in T1 relaxation of saline, correlated strongly with histological measurements of CVF [45]. In a more recent clinical study, T1 relaxation of myocardium and blood were measured dynamically before and at several points after injection of gadolinium [47]. The gadolinium partition coefficient was measured using a linear fit of myocardial R1 normalized to R1 of the blood; and from this, GDV was calculated by multiplying the gadolinium partition coefficient by (1-hematocrit/100) [47]. The authors demonstrated that in patients with diffuse fibrosis, increased LV dilation and reduced global function correlated better with increased GDV than with enhancement on LGE images [47]. The ability to detect changes in myocardial tissue composition using measurement of GDV may improve early and accurate diagnosis in patients, and may readily be applied to small animal models of diffuse fibrosis, potentially enabling more rapid evaluation of novel anti-fibrotic therapies.

In addition to imaging focal infarction and diffuse fibrosis, T2-weighted CMR of myocardial edema is emerging as a novel method for measurement of area at risk (AAR) in the presence of acute coronary syndrome (ACS) [49], as well as after MI [50–52]. Myocardial edema occurs rapidly after the onset of ischemia and areas of edema appear hyperintense on T2-weighted images of the heart [49, 51]. Example T2-weighted CMR images which highlight the AAR in a patient and a mouse are illustrated in Fig. 5. In the presence of ACS, T2-weighted imaging of edema has recently been used to visualize myocardium at risk of MI and identify patients in need of immediate coronary revascularization [49]. In the presence of MI, AAR represents the combination of infarcted myocardium and salvaged myocardium [50, 51]. In initial studies, determination of AAR by T2-weighted CMR was validated against microspheres in a dog model of MI [53], and later applied in patients after MI [52]. In a recent prospective clinical study by Berry et al., AAR as calculated by T2-weighted CMR correlated strongly with traditional angiographic measures of ischemia [51]. Furthermore, estimation of myocardial salvage, which was estimated as the differences between AAR and infarct size, was possible in all patients regardless of prior medical history [51]. The emergence of CMR methods to measure AAR will likely lead to new clinical applications in patients, as well as use in research of edema and infarct healing.

MRI of Myocardial Perfusion

Imaging of myocardial perfusion plays a critical role in the diagnosis and treatment of patients with ischemic heart disease (for a full review, see Patel et al. [54]), and is playing an increasing role in pre-clinical cardiac research. While X-ray angiography is the most commonly used method to identify occlusions of coronary arteries, first-pass contrast-enhanced CMR has become an established technique for measuring myocardial perfusion and perfusion

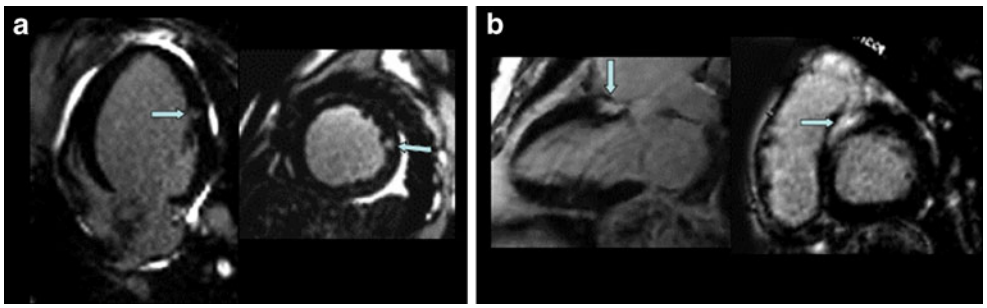

Fig. 4 LGE CMR of myocardial fibrosis. Accumulation of gadolinium in areas of fibrosis can be visualized using LGE-CMR as foci of hyperintensity (*white arrows*) in inversion recovery images. **a** Images acquired from a patient displaying predominantly mid-wall enhancement at the mid-ventricle. **b** Images from a patient displaying enhancement of the intra-ventricular septum towards the base of the heart. Patterns of focal enhancement represent regions of dense fibrosis. Images reprinted with permission from Wu et al. [15]

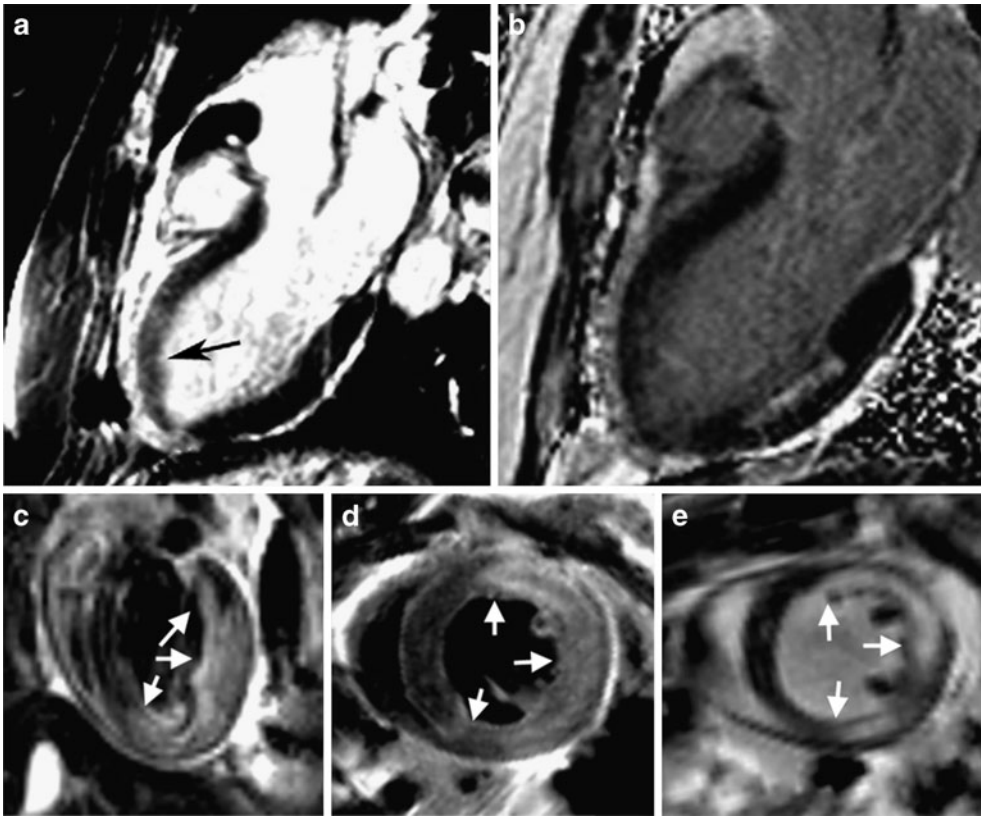

Fig. 5 T2-weighted CMR of myocardial edema and area at risk (AAR). **a** Bright-blood T2-weighted long-axis image from a patient presenting with chest pain demonstrates significant myocardial edema along the anterior wall without accompanying MI (*black arrow*) [50]. **b** LGE CMR illustrates no MI along the anterior wall, although an unrelated subendocardial posterior MI was present. **c**, **d** Black-blood T2-weighted CMR images of a mouse heart acquired using a T2-prepared sequence [138] demonstrate myocardial edema 2 days after experimental reperfused MI (*arrows*). The AAR is larger than the corresponding region of MI (**e**), and includes salvaged myocardium. Figure components reprinted with permission from West et al. [50] and Beyers et al. [138]

reserve in patients [55–58] and is emerging as a technique for use in mice [59–61]. Sample images and data from human and mouse first-pass perfusion imaging studies are shown in Fig. 6. Although first-pass perfusion imaging in patients is not new, recent improvements have included the development of dual-bolus [62] and dual-contrast [63] methods for improved quantification of the arterial input function, incorporation of compressed sensing and parallel imaging techniques to improve spatial and temporal resolution and coverage [64], and calculation of pixel-wise values of myocardial blood flow from first-pass images [65]. Implementation of first-pass perfusion imaging in mice has generally been limited by faster heart rates and the subsequent tradeoff between imaging speed and spatial resolution. However, recent studies have implemented spiral imaging (Fig. 6b) [59], segmented image acquisition and parallel imaging [61], and accelerated imaging using *k*-space and time domain undersampling with constrained reconstruction [60] to achieve adequate spatial and temporal resolution. In two of these studies, quantitative measurements of regional myocardial perfusion were made before and after MI [59, 60], making this technique appealing for use in pre-clinical studies of myocardial perfusion.

Compared to first-pass perfusion imaging, arterial spin labeling (ASL) is an emerging CMR method in both humans [66–70] and small animals [27, 42, 71–83]. The most common ASL method used in the heart, flow-sensitive alternating inversion recovery (FAIR)-ASL [74], typically uses an ECG-gated Look–Locker [84] acquisition to obtain a series of end-diastolic images at an array of TIs following slice-selective (SS) and non-selective (NS) inversions. Following SS inversion, the inflow and exchange of non-inverted blood spins into the inverted imaging slice imparts an apparent shortening effect on measured T1 ($T1_{SS}$) when compared to that measured after NS inversion ($T1_{NS}$). Based on a T1-difference approach, myocardial perfusion can be measured in units of ml/g/min as $P=(1/T1_{SS}-1/T1_{NS})*T1_{NS}/T1_{blood}*\lambda$, where λ is the blood/tissue patrician coefficient [72]. While acquisition of ASL images at a rate of one image per heart beat in humans results in sparse sampling of T1 relaxation curves, methods to sample T1 relaxation curves at higher densities have been developed [85, 86]. An additional limitation of FAIR-ASL in humans is that normal levels of myocardial perfusion, around 1 ml/g/min [10, 70], correspond to small differences between $T1_{SS}$ and $T1_{NS}$. Thus, ASL is relatively insensitive to changes in resting myocardial perfusion values in humans. However, a recent study using FAIR-ASL at a field strength of 3 T demonstrated the ability to measure perfusion in the human heart, and presented analysis of sources of noise and their impact in ASL measurements [70]. In addition, the difference between $T1_{NS}$ and $T1_{SS}$ increases with increasing field strength for a given level of

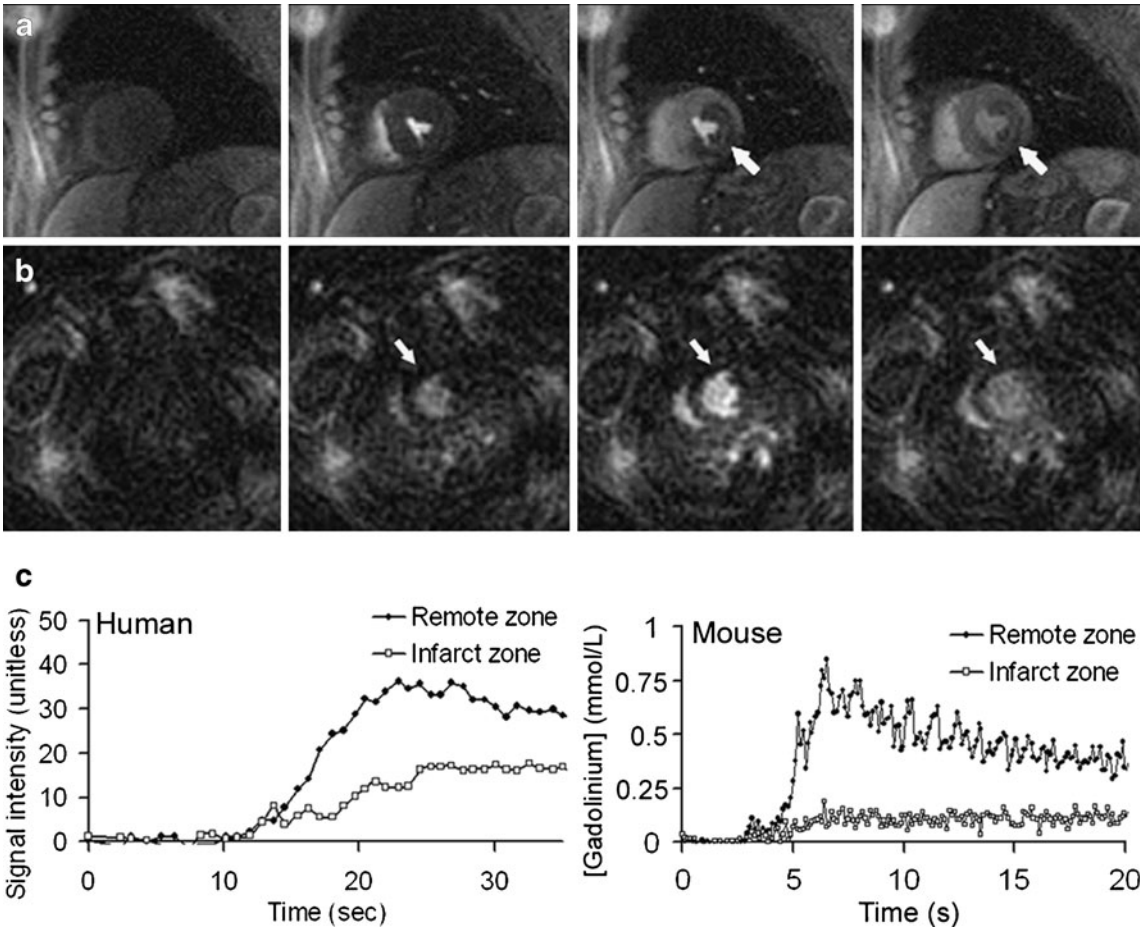

Fig. 6 First-pass CMR of myocardial perfusion in humans and mice after MI. **a** Images acquired in a patient before injection of a bolus of gadolinium, as the bolus arrives in the LV blood pool, as it transits the myocardium, and during washout (*left to right*). As the bolus of gadolinium transits the myocardium, normally perfused myocardium becomes hyperintense, while diminished myocardial perfusion causes the infarct zone to remain hypointense (*white arrow*). **b** First-pass CMR images acquired in a mouse heart demonstrate similar gadolinium kinetics to humans in infarct (*white arrow*) and remote zones of myocardium. Higher heart rates in mice necessitate faster image acquisition, resulting in relatively low resolution images. **c** Graphs of myocardial signal intensity from **a** demonstrate significant differences in the rate of signal enhancement and maximal signal enhancement between remote and infarct zones (*left*). In the mouse experiment (*right*), signal intensity is converted to gadolinium concentration as detailed by Cernicanu et al. [139]. Using such a technique, perfusion in units of $ml_{blood}/g_{tissue}/min$ can be estimated. Figure components reprinted with permission from Antkowiak et al. [59]

myocardial perfusion, suggesting that ASL measurements in the human heart may improve as higher field strength MRI systems are developed.

While FAIR-ASL has been implemented in small animals to measure myocardial perfusion in healthy tissue [27, 42, 71–73], respiratory motion artifact, variability in heart rate, and problems with ECG triggering have prevented measurement of perfusion during acute MI. Recently, we implemented a FAIR-ASL method in mice which used combined cardiac and respiratory gating during image acquisition (CRG-ASL), and sorted acquired data using a fuzzy C-means clustering algorithm prior to image reconstruction [42]. Using this method, we were able to measure regional myocardial perfusion in healing infarcts in mice. Figure 7 illustrates sample maps of myocardial perfusion acquired in a mouse 1 day after MI using CRG-ASL, as well as measurements of regional myocardial perfusion during the time–course of infarct healing. While acquisition time in ASL experiments is long compared to first-pass perfusion imaging, ASL enables measurement of perfusion in mice without the need for challenging tail vein injections, and is not limited by the rapid washout of contrast agent, enabling acquisition of high resolution perfusion maps in the mouse heart. A major target in translational cardiac research of infarct healing is restoration of healthy levels of myocardial perfusion to ischemic and remodeling tissue. As novel pro-angiogenic therapies progress from preclinical experiments to clinical application, the ability to serially measure the restoration of myocardial perfusion using either ASL or first-pass perfusion imaging will prove useful.

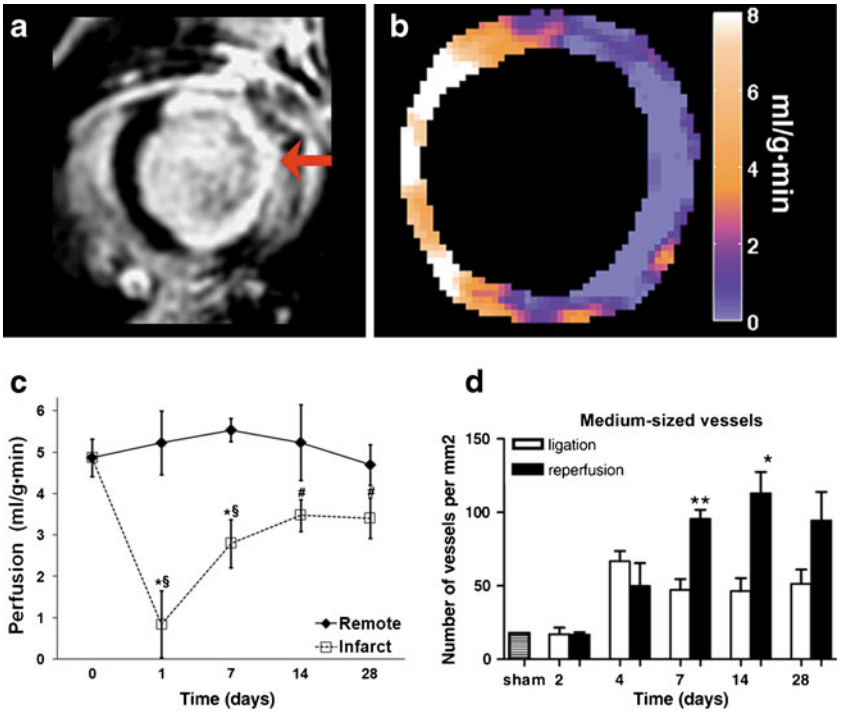

Fig. 7 Changes in myocardial perfusion during the process of infarct healing in the mouse heart as measured using FAIR-ASL. **a** LGE CMR image of a mouse heart acquired 1 day after experimental MI demonstrates hyperenhancement of the infarcted region (*red arrow*). **b** Map of myocardial perfusion generated using cardiac and respiratory gated ASL (CRG-ASL [42]) demonstrates a significant perfusion defect in close spatial agreement with the region of infarction as defined in **a**. **c** Time–course of perfusion in infarct and remote myocardium as measured using CRG-ASL. One day after MI, perfusion was very low in the infarct zone and normal in remote myocardium. Between days 1 and 14, perfusion increases in infarct zone myocardium, while remaining unchanged in remote zone myocardium (*P<0.05 vs. remote, $^{\S}P$<0.05 vs. day 1 remote, $^{\#}P$< 0.05 vs. day 1 infarct). The time–course of recovery of perfusion in infarct zone myocardium reflects changes in perfusion secondary to growth of new blood vessels (**e**, *black bars*). **d** Neovascularization of medium sized blood vessels in infarct zone myocardium was demonstrated to occur primarily between 2 and 14 days after MI in a study using a similar model of reperfused MI in mice (*P<0.05, **P<0.01, ligation vs. reperfusion). Images **a**–**d** were reprinted with permission from Vandsburger et al. [42]; **e** in the figure was reprinted with permission from Vandervelde et al. [140]

MRI of Cell Tracking and Molecular Imaging

Migration of non-resident cells into remodeling tissue as well as changes in expression of certain biomarkers are common to many cardiovascular diseases [87–89]. Traditionally, techniques such as immunohistochemical staining of tissue sections, bioluminescence imaging of labeled cells, and fluorescence microscopy with targeted ligands have been used to examine such changes in cardiovascular diseases. MRI tracking of labeled cells and targeted molecular MRI are emerging techniques for the heart and vasculature [90]. Although these techniques are mainly investigated in small animals, they have significant translational potential.

Amongst MRI cell tracking studies, cell labeling typically involves the use of either gadolinium-based agents or a variety of super-paramagnetic iron oxide (SPIO) particles. While clusters of cells labeled with gadolinium agents appear hyperintense in T1-weighted images [91], cells labeled with SPIO particles typically appear as hypointense regions on T2*-weighted images [92]. In a recent study in mice, stem cells labeled with a gadolinium-based agent were injected into infarct zone myocardium and visually tracked using T1-weighted imaging for up to 14 days [93]. In a similar study, the migration of macrophages (labeled after phagocytosis of gadolinium labeled liposomes) into the mouse heart after MI was quantitatively assessed using T1 mapping (Fig. 8) [94]. Limitations of gadolinium agents include lower sensitivity and the potential for alterations in proliferation and gene expression amongst certain cell types [95]. For these reasons, cell labeling with iron oxide particles has been more common amongst MRI cell tracking studies [92, 96, 97, 98]. Recent studies have used MRI cell tracking with iron oxide particles and T2*-weighted imaging to track both embryonic stem cells [99] (Fig. 9) and bone marrow stromal cells [100] after implantation into the infarcted rat heart, to label and track macrophages in a mouse model of MI [101], and

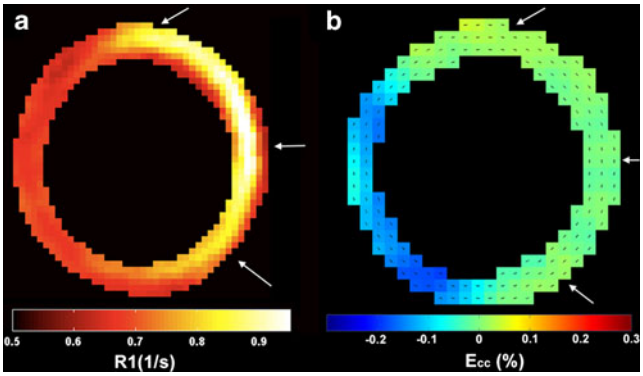

Fig. 8 CMR of gadolinium-labeled macrophages in the mouse heart after MI. **a** A relaxivity (R1) map calculated from a Look–Locker image series demonstrates enhanced R1 in the infarct zone (*white arrows*), indicating the presence of labeled macrophages. **b** A map of end-systolic E_{cc} acquired using cine DENSE in the same location delineates the infarcted region as a region of diminished contractile function. Together, these images demonstrate that macrophage infiltration is confined to the infarcted region, with greatest intensity in the core of the infarct. Figure components reprinted with permission from Naresh et al. [94]

to track cells involved in heart transplant rejection in a rat model [102]. While uncertainty remains as to whether signal loss originates from labeled cells or from other sources of signal loss [91], a number of techniques have recently emerged to produce positive contrast from cells labeled with iron oxide particles in order to improve visualization and eliminate some uncertainty [103, 104, 105]. A significant limitation to the use of iron oxide particles for cell tracking, particularly in studies of cell transplantation therapy, is the ability to distinguish between living and dead labeled cells. In a recent study, SPIO-labeled adult epicardium-derived cells, one group living and the other dead, were injected directly into the hearts of mice following MI [106]. Serial CMR imaging demonstrated similar signal voids in the vicinity of both dead and living cells over the time course of imaging, while histological examination demonstrated that iron oxide particles from dead cells were slowly absorbed by macrophages [106]. In an attempt to overcome this limitation, conditional over-expression of ferritin heavy chain (h-ferritin) to obtain T2* contrast in living cells has been explored [107, 108]. In one such study, mouse skeletal myoblasts were engineered to over express h-ferritin and were successfully tracked using T2*-weighted CMR for a period of 3 weeks after implantation in the hearts of mice with experimental MI [107]. As cell-based therapies for cardiac repair progress from pre-clinical to clinical application, CMR techniques which enable tracking of labeled cells will likely be more widely used.

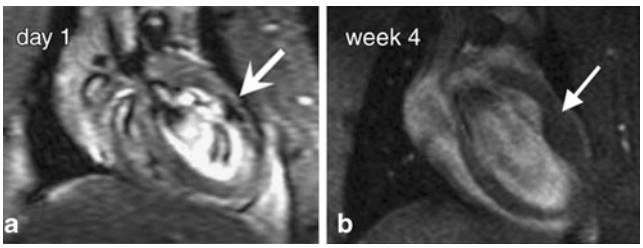

Fig. 9 CMR tracking of SPIO-labeled embryonic stem cells (ESC) for cardiac repair after MI. **a** The region of injection of SPIO labeled ESC appears as a large hypointensity (*white arrow*) compared to surrounding myocardium at 1 day after MI. **b** At 4 weeks after MI, signal loss is still observed in the same region, however, histological analysis demonstrated significant uptake of SPIO by macrophages. Figure reprinted with permission from Qiao et al. [99]

In addition to cellular imaging, molecular MRI is emerging to evaluate changes in expression of cell surface receptors, ligands, and other biomarkers common to cardiovascular disease. Recently, an increasing number of molecular MR imaging probes have been developed using principles similar to other molecular imaging modalities, namely the conjugation of an MR contrast agent to a targeted molecular probe or peptide (for full reviews, see [109–112]). In a recent study by Helm et al., a gadolinium-based collagen-targeted MRI contrast agent (EP-3533, Epix Pharmaceutical) was used to study myocardial fibrosis in chronic MI in mice [113]. Areas of fibrotic scar tissue, which appeared bright on T1-weighted CMR images, demonstrated strong correlation with regions of fibrosis as identified using picrosirius red histological staining (Fig. 10) [113]. In a separate study, a magnetoflourescent nanoparticle (AnxCLIO-Cy5.5) targeting apoptotic cardiomyocytes was used in the hearts of transgenic mice [110]. Using T2*-weighted imaging, the authors demonstrated discrete regions of hypointensity in areas identified as containing apoptotic cardiomyocytes [110]. The persistent and low levels (1–2%) of apoptosis in this mouse model are similar in heart failure patients [110], suggesting a novel mechanism by which to evaluate the presence of apoptosis in heart failure patients. While the use of targeted molecular MRI has demonstrated significant promise in preclinical studies, translation to clinical imaging has progressed more slowly. In a recent clinical study, a gadolinium-based fibrin-targeted contrast agent (EP-2104R) was used to visualize thrombi formation in the heart and vasculature in patients (Fig. 11) [114].

Manganese-Enhanced MRI of Calcium Channel Function

Ca^{2+} cycling plays a critical role in maintaining homeostatic function of the heart [115], with changes in Ca^{2+} cycling often causing or accompanying various forms of

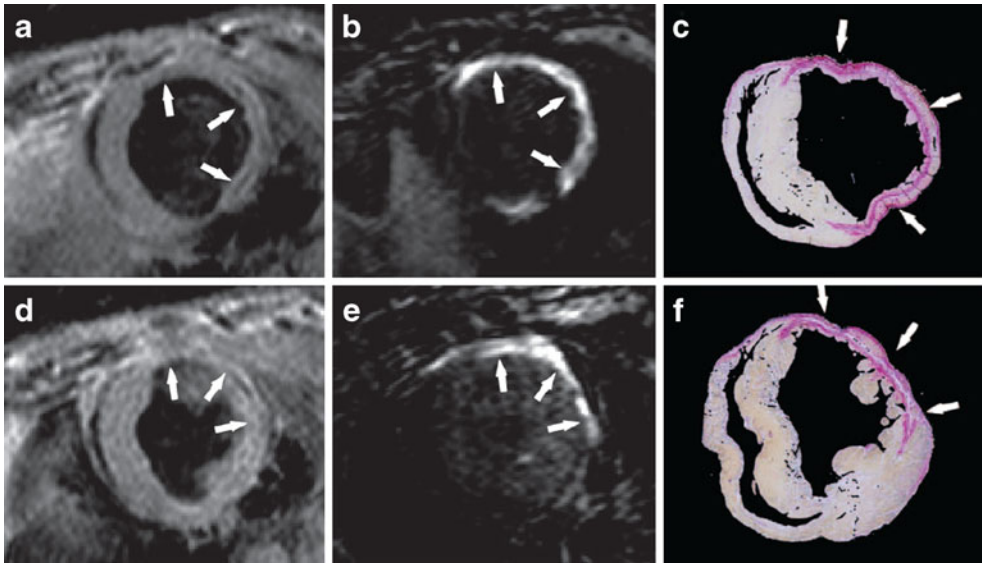

Fig. 10 Molecular MRI in mice using a collagen-targeted contrast agent: EP-3533. **a**, **d** Black-blood gradient echo images of the mouse heart at two locations, acquired 6 weeks after surgically induced MI, demonstrate a thinned LV wall in the area of the healed infarct (*white arrows*). **b**, **e** Inversion recovery images of the heart acquired 40 min after injection of EP-3533 demonstrate hyperintensity (*white arrows*) within areas of collagen-rich scar tissue. The patterns of hyperintensity (**b**, **e**) correlate closely with photomicrographs of picrosirius red-stained tissue sections (×9 magnification), in which areas of high collagen content appear red compared to surrounding myocardium (*white arrows*). Figure reprinted with permission from Helm et al. [113]

cardiomyopathy [116]. As a result, research into the roles of individual genes involved in maintaining calcium homeostasis, as well as potential therapies to restore normal calcium cycling to the failing heart have garnered significant attention. Manganese (Mn^{2+}), which is fairly similar in size and identical in charge to Ca^{2+}, enters cardiomyocytes through the trans-membrane L-type Ca^{2+} channel (LTCC) in proportion (~8%) to Ca^{2+} flux [117], and shortens T1 relaxation in relation to concentration [118]. Based on this, Mn-enhanced CMR has been used to assess LTCC function both outside [119] and inside the heart [120]. Prior studies have used Mn-enhanced CMR in the canine heart in conjunction with surgically induced MI to assess myocardial viability (Fig. 12) [121], and area at risk [122]. In the mouse heart, dynamic Mn-enhanced CMR has been used to observe changes in LTCC function during increased cardiac inotropy [123], as well as following MI [124] using a timed infusion of $MnCl_2$ and T1-weighted imaging. Recently, Mn-enhanced CMR has been used to probe changes in Ca^{2+} uptake and extrusion in the mouse heart with T1 mapping

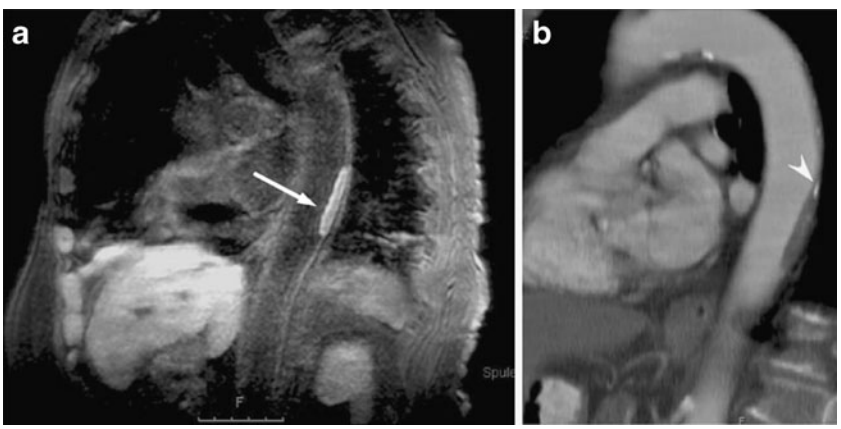

Fig. 11 Molecular imaging of the fibrin targeted contrast agent EP-2104R in the descending thoracic aorta of a human patient. **a** Inversion recovery, black-blood gradient echo image demonstrates clear hyperintensity of the forming clot (*white arrow*) within the patient's blood vessel. **b** Contrast-enhanced computed tomography image confirms the location of plaque within the aortic wall (*gray area*), as well as the presence of calcification (*white arrowhead*). Figure reprinted with permission from Spuentrup et al. [114]

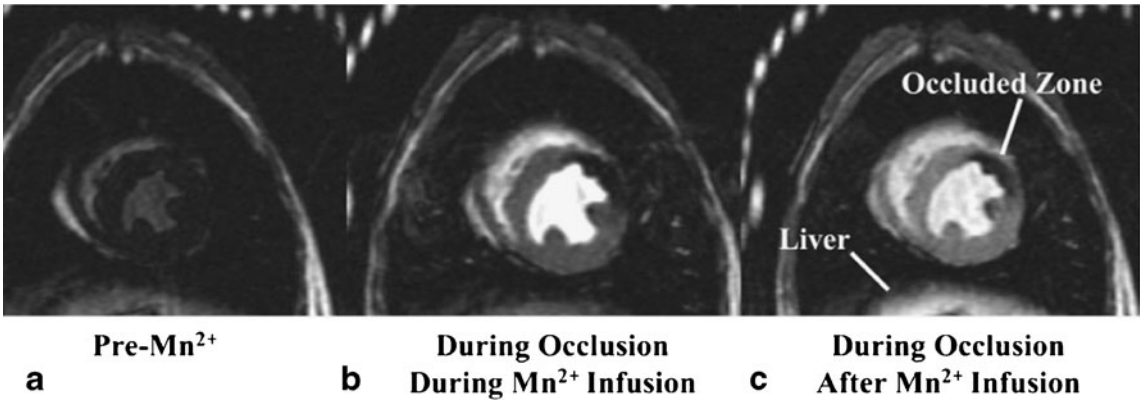

Fig. 12 Assessment of myocardial viability using Mn-enhanced CMR in the ischemic dog heart. Mid-ventricular short axis images were acquired using an inversion recovery pulse sequence. **a** Prior to infusion of Mn^{2+}, signal intensity appears uniform throughout the myocardium. **b** During Mn^{2+} infusion in the presence of induced ischemia, viable myocardium appears hyperintense compared to ischemic and necrotic myocardium. **c** While uptake of Mn^{2+} in viable myocardium is immediate, washout time is on the order of hours. Subsequently, even after the end of Mn^{2+} infusion, viable and ischemic myocardium can be clearly delineated. Figure reprinted with permission from Hu et al. [121]

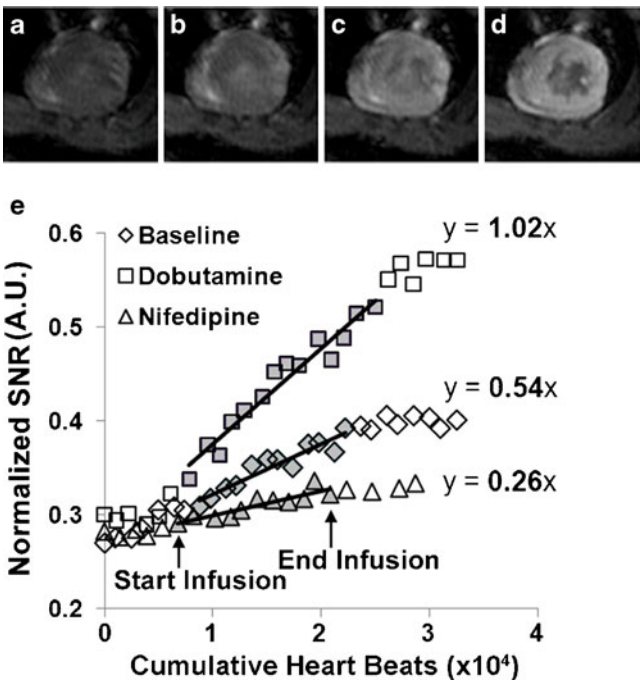

Fig. 13 Mn-enhanced CMR of the mouse heart. **a**–**d** Mid-ventricular short-axis T_1-weighted images from a mouse demonstrate increasing SNR over time during IP infusion of $MnCl_2$. Images were acquired over 90 min, while $MnCl_2$ was infused from 20 to 50 min. The specific times corresponding to each image are 15, 30, 50, and 80 min for **a**–**d**, respectively. **e** When acquiring images using the technique outlined in [127], accumulation of Mn^{2+} within cardiomyocytes results in a linear increase in SNR during infusion. The rate of increase in SNR (*solid black line*) over the points corresponding to $MnCl_2$ infusion (*filled gray* symbols between the start and end of infusion), provides an index of integrated Mn^{2+} flux through the L-type calcium channel (LTCC) (LTCCI, *bold numbers*). Sample data from one WT mouse demonstrate an increase in LTCCI over baseline in response to β-adrenergic stimulation with dobutamine, and a decrease from baseline in response to partial LTCC inhibition with nifedipine. Figure reprinted with permission from Vandsburger et al. [127]

[125, 126]. We recently used dynamic Mn-enhanced CMR and a timed infusion of $MnCl_2$ (Fig. 13) to measure a quantitative index of function (LTCCI) [127], which is analogous to the traditional in vitro measurement of LTCC current density [116], in order to elucidate the roles of different isoforms of NOS in Ca^{2+} cycling [116]. Although Mn-enhanced CMR has emerged as a powerful preclinical research tool, the potential toxicity of free Mn^{2+} remains an obstacle to clinical translation. Interestingly, a recent study in healthy human volunteers demonstrated significant myocardial T1 shortening with minimal side effects in response to a short low level infusion of $MnCl_2$ [128]. While such results are encouraging, more safety studies will be required to investigate the potential for clinical use of $MnCl_2$.

MRI of Blood Flow in Large Vessels

While this review has focused on the heart, emerging CMR methods also play a significant role in translational research in vascular diseases such as atherosclerosis. Clinically, Doppler ultrasound has been used extensively to measure blood flow velocity (BFV) in order to examine atherosclerotic progression in major blood vessels [129]. However, such BFV measurements are restricted in dimension depending upon transducer orientation [129]. Alternatively, computational fluid dynamics has been implemented to model wall shear stress (WSS) [129], which is reduced in atheroprone arteries [130]. Similarly, phase contrast (PC) MRI is an established technique that has been used to measure BFV and volume flow in two and three dimensions [129, 131]; however, measurement of WSS from such experiments has been

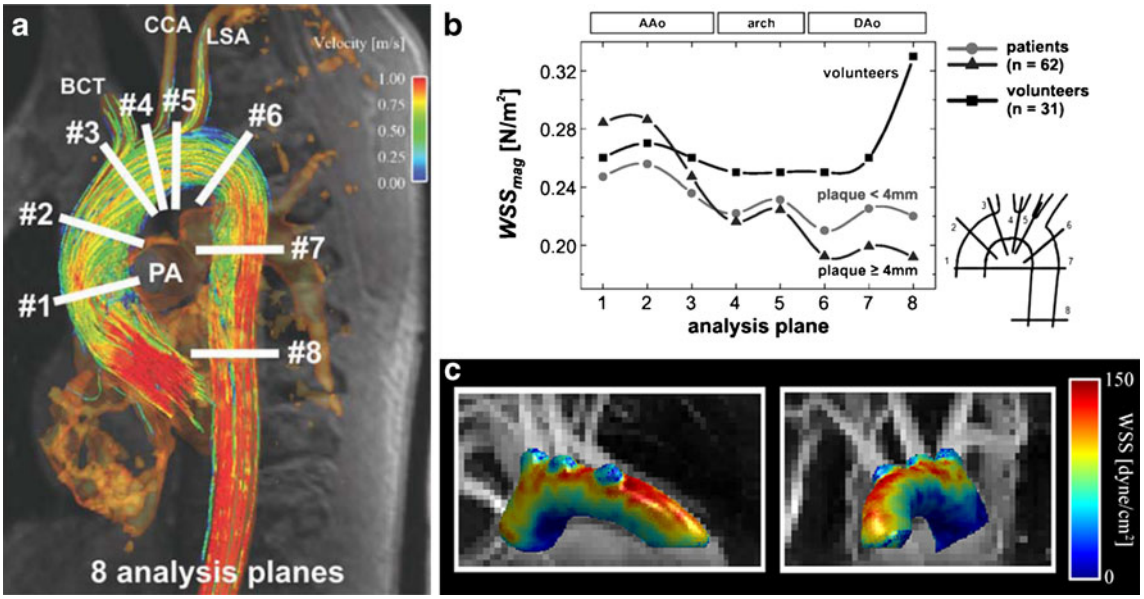

Fig. 14 Time-resolved 4D phase contrast (PC) MRI of blood flow velocity (BFV) and wall shear stress (WSS) in the human and mouse aorta. **a** Visualization of systolic 3D blood flow in the human aorta demonstrates heterogeneity in BFV. Assessment of WSS was performed along eight analysis planes (*white lines*) normal to the direction of blood flow in the ascending aorta (AAo), the aortic arch (arch), and the descending aorta (DAo). **b** Average measurements of the magnitude of WSS in healthy volunteers and patients with acute retinal or cerebral ischemia demonstrate a correlation between decreased WSS beginning at the aortic arch and plaque size. **c** 3D map of peak-systolic WSS measurements along the aortic arch in a mouse demonstrate higher WSS values near the outer radius and lower WSS values near the inner radius. Figure A,B reprinted with permission from Harloff et al. [134]; **c** in the figure was reprinted with permission from Janiczek et al. [136]

limited to regional measurement in 2D slices [132]. Recently, improvements to flow-sensitive 3D cine (or 4D) PC-CMR have led to better measurements of the 3D time-varying BFV, WSS, and oscillatory shear index (OSI) in humans [132–135] and mice [136]. In a recent pre-clinical study performed in mice, 4D PC-CMR was used to generate maps of WSS along the aortic arch (Fig. 14), which demonstrated decreased WSS along the inner radius of the aortic arch [136]. In a recent clinical study in humans, 4D PC-CMR was used to measure BFV, WSS, and OSI at eight points along the aorta in healthy volunteers and patients with atherosclerosis (Fig. 14) [134]. Compared to healthy volunteers, measurements of lower WSS magnitude along the aorta in patients correlated with the presence and size of plaque in the aortic wall (Fig. 14). Continuing improvements to these methods will enable increased use of 4D PC-CMR for assessment of atherosclerotic progression in patients, as well as for investigation of the roles of individual genes in disease development, and assessment of novel anti-atherosclerotic therapies.

Conclusions

CMR has become a powerful tool for use in translational cardiovascular research. Both emerging CMR methods and knowledge gained from preclinical experiments using CMR can be translated to clinical use. Emerging CMR techniques now enable multi-scale in vivo characterization of the heart, from changes in global LV structure and function, to changes in tissue composition, mechanics, and perfusion, and to changes in calcium channel function and gene expression. In addition, novel techniques for cell tracking and molecular imaging can be used in both clinical and preclinical research. Many of the techniques described in this review can be combined in a single imaging study, providing a comprehensive assessment of the heart as a function of disease progression or treatment. A major challenge for the future will involve translation of molecular and cellular imaging to clinical practice.

Acknowledgments Work by MHV was supported by American Heart Association pre-doctoral grant AHA0815242E, and by a postdoctoral fellowship from the Whitaker International Fellows and Scholars Program. FHE is supported by NIH R01 EB 001763. The authors would like to acknowledge the contribution of figure material from Michael Salerno, Amy West, Ron Beyers, Patrick Antkowiak, Nivedita Naresh, and Xiao Chen.

References

1. Bui, A., Horwich, T., & Fonarow, G. (2011). Epidemiology and risk profile of heart failure. *Nature Reviews Cardiology, 8*(1), 30–41.

2. Kearns-Jonker, M., & Dai, W. K. R. A. (2010). Stem cells for the treatment of heart failure. *Current Opinion in Molecular Therapeutics, 12*(4), 432–441.
3. Boyle, A., McNiece, I., & Hare, J. (2010). Mesenchymal stem cell therapy for cardiac repair. *Methods in Molecular Biology, 660*, 65–84.
4. Gepstein, L. (2010). Cell and gene therapy strategies for the treatment of postmyocardial infarction ventricular arrhythmias. *Annals of the New York Academy of Sciences, 1188*, 32–38.
5. Ruvinov, E., Leor, J., & Cohen, S. (2011). The promotion of myocardial repair by the sequential delivery of IGF-1 and HGF from an injectable alginate biomaterial in a model of acute myocardial infarction. *Biomaterials, 32*(2), 565–578.
6. Frost, R., & van Rooij, E. (2010). miRNAs as therapeutic targets in ischemic heart disease. *Journal of Cardiovascular Translational Research, 3*(3), 280–289.
7. Dobrucki, L., & Sinusas, A. (2010). PET and SPECT in cardiovascular molecular imaging. *Nature Reviews Cardiology, 7*(1), 38–47.
8. Pennell, D. J. (2010). Cardiovascular magnetic resonance. *Circulation, 121*(5), 692–705.
9. Salerno, M., & Kramer, C. (2009). Advances in cardiovascular MRI for diagnostics: Applications in coronary artery disease and cardiomyopathies. *Expert Opinion on Medical Diagnostics, 3*(6), 673–687.
10. Epstein, F. H. (2007). MR in mouse models of cardiac disease. *NMR in Biomedicine, 20*(3), 238–255.
11. Kramer, C., Rogers, W. J., Mankad, S., Theobald, T., Pakstis, D., & Hu, Y. (2000). Contractile reserve and contrast uptake pattern by magnetic resonance imaging and functional recovery after reperfused myocardial infarction. *Journal of the American College of Cardiology, 36*(6), 1835–1840.
12. Rogers, W. J., Kramer, C., Geskin, G., Hu, Y., Theobald, T., Vido, D., et al. (1999). Early contrast-enhanced MRI predicts late functional recovery after reperfused myocardial infarction. *Circulation, 99*(6), 744–750.
13. Maron, M. (2009). The current and emerging role of cardiovascular magnetic resonance imaging in hypertrophic cardiomyopathy. *Journal of Cardiovascular Translational Research, 2*(4), 415–425.
14. Epstein, F. H. (2007). MRI of left ventricular function. *Journal of Nuclear Cardiology, 14*(5), 729–744.
15. Wu, K., Weiss, R., Thiemann, D., Kitagawa, K., Schmidt, A., Dalal, D., et al. (2008). Late gadolinium enhancement by cardiovascular magnetic resonance heralds an adverse prognosis in nonischemic cardiomyopathy. *Journal of the American College of Cardiology, 51*(25), 2414–2421.
16. Power, T., Kramer, C., Shaffer, A., Theobald, T., Petruolo, S., Reichek, N., et al. (1997). Breath-hold dobutamine magnetic resonance myocardial tagging: Normal left ventricular response. *The American Journal of Cardiology, 80*(9), 1203–1207.
17. Epstein, F. H., Yang, Z., Gilson, W. D., Berr, S. S., Kramer, C. M., & French, B. A. (2002). MR tagging early after myocardial infarction in mice demonstrates contractile dysfunction in adjacent and remote regions. *Magnetic Resonance in Medicine, 48*(2), 399–403.
18. Kim, D., Gilson, W. D., Kramer, C. M., & Epstein, F. H. (2004). Myocardial tissue tracking with two-dimensional cine displacement-encoded MR imaging: Development and initial evaluation. *Radiology, 230*, 862–871.
19. Gilson, W. D., Yang, Z., French, B., & Epstein, F. (2004). Complementary displacement-encoded MRI for contrast-enhanced infarct detection and quantification of myocardial function in mice. *Magnetic Resonance in Medicine, 51*(4), 744–752.
20. Gilson, W., Yang, Z., French, B., & Epstein, F. (2005). Measurement of myocardial mechanics in mice before and after infarction using multislice displacement-encoded MRI with 3D motion encoding. *American Journal of Physiology. Heart and Circulatory Physiology, 288*, H1491–H1497.
21. Gilson, W. D., Epstein, F. H., Yang, Z., Xu, Y., Prasad, K.-M. R., Toufektsian, M.-C., et al. (2007). Borderzone contractile dysfunction is transiently attenuated and left ventricular structural remodeling is markedly reduced following reperfused myocardial infarction in inducible nitric oxide synthase knockout mice. *Journal of the American College of Cardiology, 50*(18), 1799–1807.
22. Zhong, X., Spottiswoode, B., Cowart, E., Gilson, W., & Epstein, F. H. (2006). Selective suppression of artifact-generating echoes in cine DENSE using through-plane dephasing. *Magnetic Resonance in Medicine, 56*(5), 1126–1131.
23. Zhong, X., Helm, P., & Epstein, F. (2009). Balanced multipoint displacement encoding for DENSE MRI. *Magnetic Resonance in Medicine, 61*(4), 981–988.
24. Zhong, X., Spottiswoode, B., Meyer, C., Kramer, C., & Epstein, F. H. (2010). Imaging three-dimensional myocardial mechanics using navigator-gated volumetric spiral cine DENSE MRI. *Magnetic Resonance in Medicine, 64*(4), 1089–1097.
25. Helm, P., Tseng, H., Younes, L., McVeigh, E., & Winslow, R. (2005). Ex vivo 3D diffusion tensor imaging and quantification of cardiac laminar structure. *Magnetic Resonance in Medicine, 54*(4), 850–859.
26. Sosnovik, D., Wang, R., Dai, G., Wang, T., Aikawa, E., Novikov, M., et al. (2009). Diffusion spectrum MRI tractography reveals the presence of a complex network of residual myofibers in infarcted myocardium. *Circulation Cardiovascular Imaging, 2*, 206–212.
27. Vandsburger, M. H., French, B. A., Helm, P. A., Roy, R. J., Kramer, C. M., Young, A. A., et al. (2007). Multi-parameter in vivo cardiac magnetic resonance imaging demonstrates normal perfusion reserve despite severely attenuated β-adrenergic functional response in neuronal nitric oxide synthase knockout mice. *European Heart Journal, 28*(22), 2792–2798.
28. Kramer, C., Rogers, W., Theobald, T., Power, T., Geskin, G., & Reichek, N. (1997). Dissociation between changes in intramyocardial function and left ventricular volumes in the eight weeks after first anterior myocardial infarction. *Journal of the American College of Cardiology, 30*(7), 1625–1632.
29. Young, A., French, B., Yang, Z., Cowan, B., Gilson, W., Berr, S., et al. (2006). Reperfused myocardial infarction in mice: 3D mapping of late gadolinium enhancement and strain. *Journal of Cardiovascular Magnetic Resonance, 8*(5), 685–692.
30. Hankiewicz, J., Goldspink, P., Buttrick, P., & Lewandowski, E. (2008). Principal strain changes precede ventricular wall thinning during transition to heart failure in a mouse model of dilated cardiomyopathy. *American Journal of Physiology. Heart and Circulatory Physiology, 204*(1), H330–H336.
31. Gerber, B., Darchis, J., le Polain de Waroux, J., Legros, G., Pouleur, A., Vancraeynest, D., et al. (2010). Relationship between transmural extent of necrosis and quantitative recovery of regional strains after revascularization. *Journal of the American College of Cardiology Cardiovascular Imaging, 3*(7), 720–730.
32. Bove, C. M., Gilson, W., Scott, C., Epstein, F., Yang, Z., DiMaria, J. M., et al. (2005). The angiotensin II type 2 receptor and improved adjacent region function post-MI. *Journal of Magnetic Resonance Imaging, 7*, 459–464.
33. Amado, L., Schuleri, K., Saliaris, A., Boyle, A., Helm, R., Oskouei, B., et al. (2006). Multimodality noninvasive imaging demonstrates in vivo cardiac regeneration after mesenchymal stem cell therapy. *Journal of the American College of Cardiology, 48*(10), 2116–2124.

34. Schuleri, K., Feigenbaum, G., Centola, M., Weiss, E., Zimmet, J., Turney, J., et al. (2009). Autologous mesenchymal stem cells produce reverse remodelling in chronic ischaemic cardiomyopathy. *European Heart Journal, 30*(22), 2722–2732.
35. Kramer, C., Rogers, W., Theobald, T., Power, T., Petruolo, S., & Reichek, N. (1996). Remote noninfarcted region dysfunction soon after first anterior myocardial infarction. A magnetic resonance tagging study. *Circulation, 94*(4), 660–666.
36. Liu, W., Ashford, M., Chen, J., Watkins, M., Williams, T., Wickline, S., et al. (2006). MR tagging demonstrates quantitative differences in regional ventricular wall motion in mice, rats, and men. *American Journal of Physiology. Heart and Circulatory Physiology, 291*(5), H2515–H2521.
37. Epstein, F. H., & Gilson, W. D. (2004). Displacement-encoded cardiac MRI using cosine and sine modulation to eliminate (CANSEL) artifact-generating echoes. *Magnetic Resonance in Medicine, 52*(4), 774–781.
38. Spottiswoode, B., Zhong, X., Lorenz, C., Mayosi, B., Meintjes, E., & Epstein, F. (2008). 3D myocardial tissue tracking with slice followed cine DENSE MRI. *Journal of Magnetic Resonance Imaging, 27*(5), 1019–1027.
39. Paulus, W. (2010). Novel strategies in diastolic heart failure. *Heart, 96*(14), 1147–1153.
40. Daneshvar, D., Wei, J., Tolstrup, K., Thomson, L., Shufelt, C., & Merz, C. (2010). Diastolic dysfunction: Improved understanding using emerging imaging techniques. *American Heart Journal, 160*(3), 394–404.
41. Wagner, A., Mahrholdt, H., Thomson, L., Hager, S., Meinhardt, G., Rehwald, W., et al. (2006). Effects of time, dose, and inversion time for acute myocardial infarct size measurements based on magnetic resonance imaging-delayed contrast enhancement. *Journal of the American College of Cardiology, 47*(10), 2027–2033.
42. Vandsburger, M., Janiczek, R., Xu, Y., French, B., Meyer, C., Kramer, C., et al. (2010). Improved arterial spin labeling after myocardial infarction in mice using cardaic and respiratory gated Look–Locker imaging with fuzzy C-means clustering. *Magnetic Resonance in Medicine, 63*(3), 648–657.
43. Iles, L., Pfluger, H., Phrommintikul, A., Cherayath, J., Aksit, P., Gupta, S., et al. (2008). Evaluation of diffuse myocardial fibrosis in heart failure with cardiac magnetic resonance contrast-enhanced T1 mapping. *Journal of the American College of Cardiology, 52*(19), 1574–1580.
44. Babu-Narayan, S., Kilner, P., Li, W., Moon, J., Goktekin, O., Davlouros, P., et al. (2006). Ventricular fibrosis suggested by cardiovascular magnetic resonance in adults with repaired tetralogy of fallot and its relationship to adverse markers of clinical outcome. *Circulation, 113*(3), 405–413.
45. Kehr, E., Sono, M., Chugh, S., & Jerosch-Herold, M. (2008). Gadolinium-enhanced magnetic resonance imaging for detection and quantification of fibrosis in human myocardium in vitro. *The International Journal of Cardiovascular Imaging, 24*(1), 61–68.
46. Gai, N., Turkbey, E., Nazarian, S., van der Geest, R., Liu, C., Lima, J., et al. (2010). T(1) mapping of the gadolinium-enhanced myocardium: Adjustment for factors affecting interpatient comparison. *Magnetic Resonance in Medicine*. doi:10.1002/mrm.22716.
47. Broberg, C., Chugh, S., Conklin, C., Sahn, D., & Jerosch-Herold, M. (2010). Quantification of diffuse myocardial fibrosis and its association with myocardial dysfunction in congenital heart disease. *Circulation Cardiovascular Imaging, 3*(6), 727–734.
48. Flacke, S., Fischer, S., & Lorenz, C. (2001). Measurement of the gadopentetate dimeglumine partition coefficient in human myocardium in vivo: Normal distribution and elevation in acute and chronic infarction. *Radiology, 218*, 703–710.
49. Raman, S., Simonetti, O., Winner, M., Dickerson, J., He, X., Mazzaferri, E., et al. (2010). Cardiac magnetic resonance with edema imaging identifies myocardium at risk and predicts worse outcome in patients with non-ST-segment elevation acute coronary syndrome. *Journal of the American College of Cardiology, 55*(22), 2480–2488.
50. West, A., & Kramer, C. (2010). Cardiovascular magnetic resonance imaging of myocardial infarction, viability, and cardiomyopathies. *Current Problems in Cardiology, 35*(4), 176–220.
51. Berry, C., Kellman, P., Mancini, C., Chen, M., Bandettini, W., Lowrey, T., et al. (2010). Magnetic resonance imaging delineates the ischemic area at risk and myocardial salvage in patients with acute myocardial infarction. *Circulation Cardiovascular Imaging, 3*(5), 527–535.
52. Tilak, G., Hsu, L., Hoyt, R., & Arai, A. (2008). In vivo T2-weighted magnetic resonance imaging can accurately determine the ischemic area at risk for 2-day-old nonreperfused myocardial infarction. *Investigative Radiology, 43*, 7–15.
53. Aletras, A., Tilak, G., Natanzon, A., Hsu, L., Gonzalez, F., Hoyt, R., et al. (2006). Retrospective determination of the area at risk for reperfused acute myocardial infarction with T2-weighted cardiac magnetic resonance imaging: Histopathological and displacement encoding with stimulated echoes (DENSE) functional validations. *Circulation, 113*, 1865–1870.
54. Patel, A., Epstein, F., & Kramer, C. (2008). Evaluation of the microcirculation: Advances in cardiac magnetic resonance perfusion imaging. *Journal of Nuclear Cardiology, 15*(5), 698–708.
55. Gerber, B., Raman, S., Nayak, K., Epstein, F. H., Ferreira, P., Axel, L., et al. (2008). Myocardial first-pass perfusion cardiovascular magnetic resonance: history, theory, and current state of the art. *Journal of Cardiovascular Magnetic Resonance, 10*(18).
56. Jerosch-Herold, M. (2010). Quantification of myocardial perfusion by cardiovascular magnetic resonance. *Journal of Cardiovascular Magnetic Resonance, 12*, 57-.
57. Atkinson, D., Burstein, D., & Edelman, R. (1990). First-pass cardiac perfusion: Evaluation with ultrafast MR imaging. *Radiology, 173*(3–1), 757–762.
58. Patel, A., Antkowiak, P., Nadalur, K., West, A., Salerno, M., Arora, V., et al. (2010). Assessment of advanced coronary artery disease: Advantages of quantitative cardiac magnetic resonance perfusion analysis. *Journal of the American College of Cardiology, 56*(7), 561–569.
59. Antkowiak, P., Janiczek, R., Gibberman, L., Xu, C., Kramer, C., Meyer, C., et al. (2010). Quantitative first-pass perfusion MRI of the mouse heart. *Journal of Cardiovascular Magnetic Resonance, 12*(1), M10.
60. Makowski, M., Jansen, C., Webb, I., Chiribiri, A., Nagel, E., Botnar, R., et al. (2010). First-pass contrast-enhanced myocardial perfusion MRI in mice on a 3-T clinical MR scanner. *Magnetic Resonance in Medicine, 64*(6), 1592–1598.
61. Coolen, B., Moonen, R., Paulis, L., Geelen, T., Nicolay, K., & Strijkers, G. (2010). Mouse myocardial first-pass perfusion MR imaging. *Magnetic Resonance in Medicine, 64*(6), 1658–1663.
62. Christian, T., Rettmann, D., Aletras, A., Liao, S., Taylor, J., Balaban, R., et al. (2004). Absolute myocardial perfusion in canines measured by using dual-bolus first-pass MR imaging. *Radiology, 232*(3), 677–684.
63. Gatehouse, P., Elkington, A., Ablitt, N., Yang, G., Pennell, D., & Firmin, D. (2004). Accurate assessment of the arterial input function during high-dose myocardial perfusion cardiovascular magnetic resonance. *Journal of Magnetic Resonance Imaging, 20*(1), 39–45.
64. Otazo, R., Kim, D., Axel, L., & Sodickson, D. (2010). Combination of compressed sensing and parallel imaging for highly accelerated first-pass cardiac perfusion MRI. *Magnetic Resonance in Medicine, 64*(3), 767–776.

65. Goldstein, T., Jerosch-Herold, M., Misselwitz, B., Zhang, H., Gropler, R., & Zheng, J. (2008). Fast mapping of myocardial blood flow with MR first-pass perfusion imaging. *Magnetic Resonance in Medicine, 59*(6), 1394–1400.
66. Fidler, F., Wacker, C., Dueren, C., Weigel, M., Jakob, P., & Bauer, W. A. H. (2004). Myocardial perfusion measurements by spin-labeling under different vasodynamic states. *Journal of Cardiovascular Magnetic Resonance, 6*(2), 509–516.
67. Northrup, B. E., McCommis, K. S., Zhang H., Ray, S., Woodard, P. K., Groplet, R.J., et al. (2008). Resting myocardial perfusion quantification with CMR arterial spin labeling at 1.5T 3.0T. *Journal of Cardiovascular Magnetic Resonance, 10*(53).
68. Poncelet, B. P., Koelling, T. M., Schmidt, C. J., Kwong, K. K., Reese, T. G., Ledden, P., et al. (1999). Measurement of human myocardial perfusion by double-gated flow alternating inversion recovery EPI. *Magnetic Resonance in Medicine, 41*(3), 510–519.
69. Wacker, C. M., Fidler, F., Dueren, C., Hirn, S., Jakob, P. M., Ertl, G., et al. (2003). Quantitative assessment of myocardial perfusion with a spin-labeling technique: Preliminary results in patients with coronary artery disease. *Journal of Magnetic Resonance Imaging, 18*(5), 555–560.
70. Zun, Z., Wong, E., & Nayak, K. (2009). Assessment of myocardial blood flow (MBR) in humans using aterial spin labeling (ASL): Feasibility and noise analysis. *Magnetic Resonance in Medicine, 62*(4), 975–983.
71. Streif, J. U. G., Nahrendorf, M., Hiller, K.-H., Waller, C., Wiesmann, F., Rommel, E., et al. (2005). In vivo assessment of absolute perfusion and intracapillary blood volume in the murine myocardium by spin labeling magnetic resonance imaging. *Magnetic Resonance in Medicine, 53*(3), 584–592.
72. Kober, F., Iltis, I., Cozzone, P. J., & Bernard, M. (2005). Myocardial blood flow mapping in mice using high-resolution spin labeling magnetic resonance imaging: Influence of ketamine/xylazine and isoflurane anesthesia. *Magnetic Resonance in Medicine, 53*(3), 601–606.
73. Nahrendorf, M., Streif, J. U., Hiller, K.-H., Hu, K., Nordbeck, P., Ritter, O., et al. (2006). Multimodal functional cardiac MRI in creatine kinase-deficient mice reveals subtle abnormalities in myocardial perfusion and mechanics. *American Journal of Physiology. Heart and Circulatory Physiology, 290*(6), H2516–H2521.
74. Kober, F., Iltis, I., Izquierdo, M., Desrois, M., Ibarrola, D., Cozzone, P. J., et al. (2004). High-resolution myocardial perfusion mapping in small animals in vivo by spin-labeling gradient-echo imaging. *Magnetic Resonance in Medicine, 51*(1), 62–67.
75. Waller, C., Engelhorn, T., Hiller, K.-H., Heusch, G., Ertl, G., Bauer, W. R., et al. (2005). Impaired resting perfusion in viable myocardium distal to chronic coronary stenosis in rats. *American Journal of Physiology. Heart and Circulatory Physiology, 288* (6), H2588–H2593.
76. Waller, C., Hiller, K.-H., Kahler, E., Hu, K., Nahrendorf, M., Voll, S., et al. (2001). Serial magnetic resonance imaging of microvascular remodeling in the infarcted rat heart. *Circulation, 103*(11), 1564–1569.
77. Waller, C., Hiller, K.-H., Pfaff, D., Gattenlöhner, S., Ertl, G., & Bauer, W. R. (2008). Functional mechanisms of myocardial microcirculation in left ventricular hypertrophy: A hypothetical model of capillary remodeling post myocardial infarction. *Microvascular Research, 75*(1), 104.
78. Waller, C., Hiller, K.-H., Rudiger, T., Kraus, G., Konietzko, C., Hardt, N., et al. (2005). Noninvasive imaging of angiogenesis inhibition following nitric oxide synthase blockade in the ischemic rat heart in vivo. *Microcirculation, 12*(4), 339–347.
79. Waller, C., Kahler, E., Hiller, K.-H., Hu, K., Nahrendorf, M., Voll, S., et al. (2000). Myocardial perfusion and intracapillary blood volume in rats at rest and with coronary dilatation: MR imaging in vivo with use of a spin-labeling technique. *Radiology, 215*(1), 189–197.
80. Belle, V., Kahler, E., Waller, C., Rommel, E., Voll, S., Hiller, K., et al. (1998). In vivo quantitative mapping of cardiac perfusion in rats using a noninvasive MR spin-labeling method. *Journal of Magnetic Resonance Imaging, 8*, 1240–1245.
81. Iltis, I., Kober, F., Dalmasso, C., Cozzone, P. J., & Bernard, M. (2005). Noninvasive characterization of myocardial blood flow in diabetic, hypertensive, and diabetic and hypertensive rats using spin-labeling MRI. *Microcirculation, 12*(8), 607–614.
82. Iltis, I., Kober, F., Dalmasso, C., Lan, C., Cozzone, P. J., & Bernard, M. (2005). In vivo assessment of myocardial blood flow in rat heart using magnetic resonance imaging: Effect of anesthesia. *Journal of Magnetic Resonance Imaging, 22*(2), 242–247.
83. Iltis, I., Kober, F., Desrois, M., Dalmasso, C., Lan, C., Portha, B., et al. (2005). Defective myocardial blood flow and altered function of the left ventricle in type 2 diabetic rats: A noninvasive in vivo study using perfusion and cine magnetic resonance imaging. *Investigative Radiology, 40*(1), 19–26.
84. Look, D., & Locker, D. (1970). Time saving in measurement of NMR and EPR relaxation times. *The Review of Scientific Instruments, 41*, 250–251.
85. Messroghli, D., Radjenovic, A., Kozerke, S., Higgins, D., Sivananthan, M., & Ridgway, J. (2004). Modified Look–Locker inversion recovery (MOLLI) for high-resolution T1 mapping of the heart. *Magnetic Resonance in Medicine, 52*(1), 141–146.
86. Messroghli, D., Walters, K., Plein, S., Sparrow, P., Friedrich, M., Ridgway, J., et al. (2007). Myocardial T1 mapping: Application to patients with acute and chronic myocardial infarction. *Magnetic Resonance in Medicine, 58*(1), 34–40.
87. Sutton, M. G. S. J., & Sharpe, N. (2000). Left ventricular remodeling after myocardial infarction: Pathophysiology and therapy. *Circulation, 101*(25), 2981–2988.
88. Frangogiannis, N. G. (2006). The mechanistic basis of infarct healing. *Antioxidants Redox Signaling, 8*(11), 1907–1939.
89. Frangogiannis, N. G. (2008). The immune system and cardiac repair. *Pharmacological Research, 58*(2), 88.
90. Kraitchman, D., Kedziorek, D., & Bulte, J. (2011). MR imaging of transplanted stem cells in myocardial infarction. *Methods in Molecular Biology, 680*, 141–152.
91. Kraitchman, D., & Caravan, P. (2009). Magnetic resonance labeling of stem cells: Is positive tracking a plus or a minus? *Journal of the American College of Cardiology Cardiovascular Imaging, 2*(9), 1123–1125.
92. Bulte, J., Arbab, A., Douglas, T., & Frank, J. (2004). Preparation of magnetically labeled cells for cell tracking by magnetic resonance imaging. *Methods in Enzymology, 386*, 275–299.
93. Adler, E., Bystrup, A., Briley-Saebo, K., Mani, V., Young, W., Giovanonne, S., et al. (2009). In vivo detection of embryonic stem cell-derived cardiovascular progenitor cells using Cy3-labeled gadofluorine M in murine myocardium. *Journal of the American College of Cardiology Cardiovascular Imaging, 2*(9), 1114–1122.
94. Naresh, N., Vandsburger, M., Klibanov, A., Beyers, R., Antkowiak, P., Xu, Y., et al. (2010). Serial quantitative cellular MRI of macrophage infiltration in the post-infarct heart using T1-mapping and Gd-liposomes. *Circulation, 122*, A17344.
95. Bhagavathula, N., Dame, M., Dasilva, M., Jenkins, W. A., Aslam, M., Perone, P., et al. (2010). Fibroblast response to gadolinium: Role for platelet-derived growth factor receptor. *Investigative Radiology, 45*(12), 769–777.
96. Yuxiang, Y., & Bogaert, J. (2008). Cell therapy in moycardial infarction: Emphasis on the role of MRI. *European Radiology, 18*, 548–569.

97. Shapiro, E., Sharer, K., Skrtic, S., & Koretsky, A. (2006). In vivo detection of single cells by MRI. *Magnetic Resonance in Medicine, 55*(2), 242.
98. Shapiro, E., Skrtic, S., & Koretsky, A. (2005). Sizing it up: Cellular MRI using micron-sized iron oxide particles. *Magnetic Resonance in Medicine, 53*(2), 329–338.
99. Qiao, H., Zhang, H., Zheng, Y., Ponde, D., Shen, D., Gao, F., et al. (2009). Embryonic stem cell grafting in normal and infarcted myocardium: Serial assessment with MR imaging and PET dual detection. *Radiology, 250*(3), 821–829.
100. Carr, C., Stuckey, D., Tatton, L., Tyler, D., Hale, S., Sweeney, D., et al. (2008). Bone marrow-derived stromal cells home to and remain in the infarcted rat heart but fail to improve function: An in vivo cine-MRI study. *American Journal of Physiology. Heart and Circulatory Physiology, 295*(2), H533–H542.
101. Sosnovik, D., Nahrendorf, M., Deliolanis, N., Novikov, M., Aikawa, E., Josephson, L., et al. (2007). Fluorescence tomography and magnetic resonance imaging of myocardial macrophage infiltration in infarcted myocardium in vivo. *Circulation, 115*(11), 1384–1391.
102. Wu, Y., Ye, Q., Sato, K., Foley, L., Hitchens, T., & Ho, C. (2009). Noninvasive evaluation of cardiac allograft rejection by cellular and functional cardiac magnetic resonance. *JACC Cardiovascular Imaging, 2*(6), 731–741.
103. Stuber, M., Gilson, W., Schär, M., Kedziorek, D., Hofmann, L., Shah, S., et al. (2007). Positive contrast visualization of iron oxide-labeled stem cells using inversion-recovery with ON-resonant water suppression (IRON). *Magnetic Resonance in Medicine, 58*(5), 1072–1077.
104. Zhou, R., Idiyatullin, D., Moeller, S., Corum, C., Zhang, H., Qiao, H., et al. (2010). SWIFT detection of SPIO-labeled stem cells grafted in the myocardium. *Magnetic Resonance in Medicine, 63*(5), 1154–1161.
105. Liu, W., Dahnke, H., Jordan, E., Schaeffter, T., & Frank, J. (2008). In vivo MRI using positive-contrast techniques in detection of cells labeled with superparamagnetic iron oxide nanoparticles. *NMR in Biomedicine, 21*(3), 242–250.
106. Winter, E., Hogers, B., van der Graaf, L., Gittenberger-de Groot, A., Poelmann, R., & van der Weerd, L. (2010). Cell tracking using iron oxide fails to distinguish dead from living transplanted cells in the infarcted heart. *Magnetic Resonance in Medicine, 63*(3), 817–821.
107. Naumova, A., Reinecke, H., Yarnykh, V., Deem, J., Yuan, C., & Murry, C. (2010). Ferritin overexpression for noninvasive magnetic resonance imaging-based tracking of stem cells transplanted into the heart. *Molecular Imaging, 9*(4), 201–210.
108. Cohen, B., Dafni, H., Meir, G., Harmelin, A., & Neeman, M. (2005). Ferritin as an endogenous MRI reporter for noninvasive imaging of gene expression in C6 glioma tumors. *Neoplasia, 7*(2), 109–117.
109. Uppal, R., & Caravan, P. (2010). Targeted probes for cardiovascular MR imaging. *Future Medicinal Chemistry, 2*(3), 451–470.
110. Sosnovik, D., & Caravan, P. (2009). Molecular MRI of atherosclerotic plaque with targeted contrast agents. *Current Cardiovascular Imaging, 2*(2), 87–94.
111. Caravan, P. (2009). Protein-targeted gadolinium-based magnetic resonance imaging (MRI) contrast agents: Design and mechanism of action. *Accounts of Chemical Research, 42*(7), 851–862.
112. Oostendorp, M., Douma, K., Wagenaar, A., Slenter, J., Hackeng, T., van Zandvoort, M., et al. (2010). Molecular magnetic resonance imaging of myocardial angiogenesis after acute myocardial infarction. *Circulation, 121*(6), 775–783.
113. Helm, P. A., Caravan, P., French, B. A., Jacques, V., Shen, L., Xu, Y., et al. (2008). Postinfarction myocardial scarring in mice: Molecular MR imaging with use of a collagen-targeting contrast agent. *Radiology, 247*(3), 788–796.
114. Spuentrup, E., Botnar, R., Wiethoff, A., Ibrahim, T., Kelle, S., Katoh, M., et al. (2008). MR imaging of thrombi using EP-2140R, a fibrin-specific contrast agent: Initial results in patients. *European Radiology, 18*(9), 1995–2005.
115. Bers, D. M. (2008). Calcium cycling and signaling in cardiac myocytes. *Annual Review of Physiology, 70*(1), 23–49.
116. Bers, D. M. (2006). Altered cardiac myocyte calcium regulation in heart failure. *The Journal of Physiology, 21*, 380–387.
117. Masumiya, H., Tsujikawa, H., Hino, N., & Ochi, R. (2003). Modulation of manganese currents by 1,4-dihydropyridines, isoproterenol, and foskolin in rabbit ventricular cells. *Pflügers Archiv - European Journal of Physiology, 446*, 695–701.
118. Hu, T., Chuang, K., Yanasak, N., & Koretsky, A. (2011). Relationship between blood and myocardium manganese levels during manganese-enhanced MRI (MEMRI) with T(1) mapping in rats. *NMR in Biomedicine, 24*(1), 46–53.
119. Koretsky, A., & Silva, A. (2004). Manganese-enhanced magnetic resonance imaging (MEMRI). *NMR in Biomedicine, 17*(8), 527–531.
120. Wendland, M. (2004). Applications of manganese-enhanced magnetic resonance imaging (MEMRI) to imaging of the heart. *NMR in Biomedicine, 17*(8), 581–594.
121. Hu, T. C., Christian, T. F., Aletras, A. H., Taylor, J. L., Koretsky, A. P., & Arai, A. E. (2005). Manganese enhanced magnetic resonance imaging of normal and ischemic canine heart. *Magnetic Resonance in Medicine, 54*(1), 196–200.
122. Natanzon, A., Aletras, A., Hsu, L., & Arai, A. (2005). Determining canine myocardial area at risk with manganese-enhanced MR imaging. *Radiology, 236*(3), 859–866.
123. Hu, T. C. C., Pautler, R. G., MacGowan, G. A., & Koretsky, A. P. (2001). Manganese-enhanced MRI of mouse heart during changes in inotropy. *Magnetic Resonance in Medicine, 46*(5), 884–890.
124. Hu, T., Bao, W., Lenhard, S., Schaeffer, T., Yue, T., Willette, R., et al. (2004). Simultaneous assessment of left-ventricular infarction size, function and tissue viability in a murine model of myocardial infarction by cardiac manganese-enhanced magnetic resonance imaging (MEMRI). *NMR in Biomedicine, 17*(8), 620–626.
125. Waghorn, B., Edwards, T., Yang, Y., Chuang, K., Yanasak, N., & Hu, T. (2008). Monitoring dynamic alterations in calcium homeostasis by T (1)-weighted and T (1)-mapping cardiac manganese-enhanced MRI in a murine myocardial infarction model. *NMR in Biomedicine, 21*(10), 1102–1111.
126. Waghorn, B., Yang, Y., Baba, A., Matsuda, T., Schumacher, A., Yanasak, N., et al. (2009). Assessing manganese efflux using SEA0400 and cardiac T1-mapping manganese-enhanced MRI in a murine model. *NMR in Biomedicine, 22*(8), 874–881.
127. Vandsburger, M., French, B., Kramer, C., & Epstein, F. H. (2010). Cine DENSE and manganese-enhanced MRI demonstrate that nNOS, and not eNOS, plays a dominant role in modulating EC-coupling in the mouse heart. *Circulation, 122*, A12386.
128. Fernandes, J., Storey, P., da Silva, J., de Figueiredo, G., Kalaf, J., & Coelho, O. (2011). Preliminary assessment of cardiac short term safety and efficacy of manganese chloride for cardiovascular magnetic resonance in humans. *Journal of Cardiovascular Magnetic Resonance, 13*(1), 6. epub ahead of print.
129. Markl, M., Kilner, P., & Ebbers, T. (2011). Comprehensive 4D velocity mapping of the heart and great vessels by cardiovascular magnetic resonance. *Journal of Cardiovascular Magnetic Resonance, 13*(1), 7–29.
130. Caro, C. G. (2009). Discovery of the role of wall shear in atherosclerosis. *Arteriosclerosis, Thrombosis, and Vascular Biology, 29*(2), 158–161.
131. Gelfand, B., Epstein, F. H., & Blackman, B. (2006). Spatial and spectral heterogeneity of time-varying shear stress profiles in the

carotid bifurcation by phase-contrast MRI. *Journal of Magnetic Resonance Imaging, 24*(6), 1386–1392.
132. Markl, M., Wegent, F., Zech, T., Bauer, S., Strecker, C., Schumacher, M., et al. (2010). In vivo wall shear stress distribution in the carotid artery: Effect of bifurcation geometry, internal carotid artery stenosis, and recanalization therapy. *Circulation Cardiovascular Imaging, 3*(6), 647–655.
133. Markl, M., Geiger, J., Kilner, P., Föll, D., Stiller, B., Beyersdorf, F., et al. (2011). Time-resolved three-dimensional magnetic resonance velocity mapping of cardiovascular flow paths in volunteers and patients with Fontan circulation. *European Journal of Cardiothoracic Surgery, 39*(2), 206–212.
134. Harloff, A., Nussbaumer, A., Bauer, S., Stalder, A., Frydrychowicz, A., Weiller, C., et al. (2010). In vivo assessment of wall shear stress in the atherosclerotic aorta using flow-sensitive 4D MRI. *Magnetic Resonance in Medicine, 63*(6), 1529–1536.
135. Harloff, A., Albrecht, F., Spreer, J., Stalder, A., Bock, J., Frydrychowicz, A., et al. (2009). 3D blood flow characteristics in the carotid artery bifurcation assessed by flow-sensitive 4D MRI at 3 T. *Magnetic Resonance in Medicine, 61*(1), 65–74.
136. Janiczek, R., Meyer, C., Acton, S. T., Blackman, B., & Epstein, F. H. (2009). 4D spiral phase-contrast MRI of wall shear stress in the mouse aorta. *Procedings of the International Society of Magnetic Resonance in Medicine, 17*, 3857.
137. Berr, S. S., Roy, R. J., French, B. A., Yang, Z., Gilson, W., Kramer, C. M., et al. (2005). Black blood gradient echo cine magnetic resonance imaging of the mouse heart. *Magnetic Resonance in Medicine, 53*(5), 1074–1079.
138. Beyers, R., Smith, R., Xu, Y., Piras, B., Berr, S., Meyer, C., Kramer, C., French, B., Epstein, F. H. (2011). T2-weighted MRI of post-infarct myocardial edema in mice. *Magnetic Resonance in Medicine* (in press)
139. Cernicanu, A., & Axel, L. (2006). Theory-based signal calibration with single-point T1 measurements for first-pass quantitative perfusion MRI studies. *Academic Radiology, 13*(6), 686–693.
140. Vandervelde, S., van Amerongen, M. J., Tio, R. A., Petersen, A. H., van Luyn, M. J. A., & Harmsen, M. C. (2006). Increased inflammatory response and neovascularization in reperfused vs. nonreperfused murine myocardial infarction. *Cardiovascular Pathology, 15*(2), 83.